EDGE ARTICLE

Check for updates

Topology- and wavelength-governed CO$_2$ reduction photocatalysis in molecular catalyst-metal–organic framework assemblies†

Philip M. Stanley, ‡[a] Karina Hemmer, ‡[a] Markus Hegelmann,[a] Annika Schulz,[a] Mihyun Park,[a] Martin Elsner,[b] Mirza Cokoja[a] and Julien Warnan *[a]

Optimising catalyst materials for visible light-driven fuel production requires understanding complex and intertwined processes including light absorption and catalyst stability, as well as mass, charge, and energy transport. These phenomena can be uniquely combined (and ideally controlled) in porous host–guest systems. Towards this goal we designed model systems consisting of molecular complexes as catalysts and porphyrin metal–organic frameworks (MOFs) as light-harvesting and hosting porous matrices. Two MOF-rhenium molecule hybrids with identical building units but differing topologies (PCN-222 and PCN-224) were prepared including photosensitiser-catalyst dyad-like systems integrated *via* self-assembled molecular recognition. This allowed us to investigate the impact of MOF topology on solar fuel production, with PCN-222 assemblies yielding a 9-fold turnover number enhancement for solar CO$_2$-to-CO reduction over PCN-224 hybrids as well as a 10-fold increase compared to the homogeneous catalyst-porphyrin dyad. Catalytic, spectroscopic and computational investigations identified larger pores and efficient exciton hopping as performance boosters, and further unveiled a MOF-specific, wavelength-dependent catalytic behaviour. Accordingly, CO$_2$ reduction product selectivity is governed by selective activation of two independent, circumscribed or delocalised, energy/electron transfer channels from the porphyrin excited state to either formate-producing MOF nodes or the CO-producing molecular catalysts.

Introduction

Against the backdrop of increasing global energy requirements, photocatalysis has the potential to reduce the necessary energy for feedstock production and to transform waste into valuable feedstocks.[1] Solar fuel production, merging solar energy harvesting with subsequent chemical energy conversion, is a pertinent route towards such artificial photosynthesis.[2] The latter motivates bio-inspired molecular catalysts, fine-tuned to maximise selectivity and atom efficiency while minimising activation energy barriers.[3,4] However, these are often mired by limited stability and device integrability, as well as modest light-harvesting efficiency for photocatalytic systems operating under broad-spectrum irradiation.[1] Accordingly, current efforts synergise material and catalyst co-design to enable energy-

intense reactions, such as selective CO$_2$ reduction, in light-absorbing hybrids.[3,4]

Here, metal–organic framework (MOF) materials show promise due to their highly controllable chemical and (photo) physical properties enabled by their modular assembly.[5] This unlocks a breadth of differing porosities, topologies, pore sizes, guest inclusion opportunities, optoelectronic properties, and more, which intertwine and deeply condition reaction environments.[6–8] Thus, combining molecular catalysts and MOFs to heterogeneous hybrids enables catalyst stabilisation and recyclability while also gaining control over its proximal and global environment.[7,9,10] While previous reports on heterogeneous thermal MOF catalysis demonstrated that nanoreactors built by pore walls affect reaction activity, selectivity, and substrate diffusion to active sites,[8,11] these findings are not generally transferable to systems with light-driven catalysis, cascade electroreductions or defined molecular complexes as the active species. Accordingly, challenges remain in the conceptual understanding of the intrinsic effects of a MOF pore environment on such molecular MOF hybrids towards rational design of effective materials for photocatalysis. Although a few studies have investigated pore size variation, topology-based substrate orientation, and active site distance optimisation, these parameters remain poorly understood and systematic studies

[a]*Chair of Inorganic and Metal–Organic Chemistry, Department of Chemistry, TUM School of Natural Sciences, Catalysis Research Center (CRC), Technical University of Munich, Garching, Germany. E-mail: julien.warnan@tum.de*

[b]*Chair of Analytical Chemistry and Water Chemistry, Department of Chemistry, TUM School of Natural Sciences, Technical University of Munich, Garching, Germany*

† Electronic supplementary information (ESI) available: Full experimental details, analysis method description, and supplementary figures and tables. See DOI: https://doi.org/10.1039/d2sc03097g
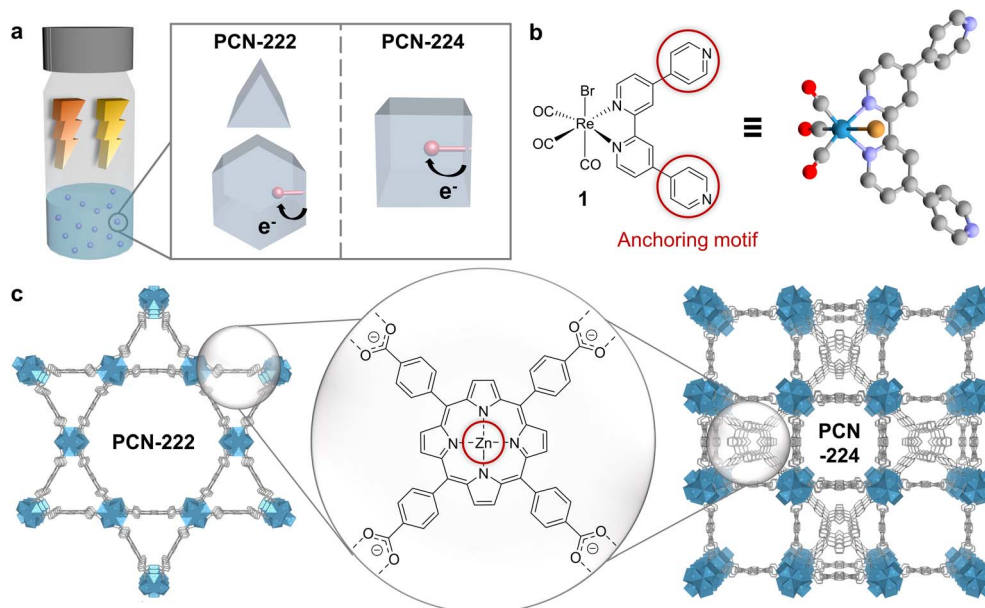
‡ These authors contributed equally.

Fig. 1 Components and structures of the assemblies. (a) Conceptual representation of the designed and synthesised materials to study the influence of MOF topology and irradiation wavelength on colloidal photocatalytic CO_2 reduction with dyadic Re-based assemblies in PCN-222 and PCN-224. Blue spheres: MOFs. Red spheres: molecular catalyst. (b) Left: Chemical structure of $ReBr(CO)_3(qtpy)$ (**1**). Circles: Pyridine anchoring motif for dyad formation. Right: DFT-optimised structure of **1**. Red: oxygen, grey: carbon, purple: N, gold: Br, cyan: Re. H atoms omitted for clarity. (c) Structures of the MOFs PCN-222 (left) and PCN-224 (right), showcasing their differing topologies but identical building blocks (porphyrin-based linkers and Zr_6-oxo-based nodes). Red: Zn anchoring motif for dyadic formation via $Zn-N_{(pyridine)}$ bonds. Rendered from CCDC 893545 and 1001133.

on how MOF topology influences properties and solar fuel performances are needed.[12–14]

Herein, we designed two supramolecular MOF-catalyst hybrids constructed from identical building blocks but differing in topology (Fig. 1a). The assemblies consist of a *fac*-$ReBr(CO)_3(qtpy)$ (**1**, qtpy = 4,4′:2′,2″:4″,4‴-quaterpyridine) CO_2 reduction catalyst and Zn-metalated 5,10,15,20-tetrakis(4-carboxylphenyl)porphyrin (**2-Zn**) linker- and Zr_6-oxo node-based MOFs, *i.e.*, PCN-222 and PCN-224 (Fig. 1b and c). These MOFs were chosen as model systems for their broad visible-light absorption,[15–18] and their reported directional exciton migration and energy funnelling to acceptors.[19,20] While **1** has not been applied in photocatalytic CO_2 reduction to date, its derivatives are known for selective CO formation under homogeneous and heterogeneous conditions, with turnover numbers (TONs) ranging from ∼10 to 4500 in the presence of sacrificial electron donors (SEDs).[9,21–23]

The MOF hosts, PCN-222 and PCN-224, were synthesised with high crystallinity, Zn metalated and then post-synthetically linker-functionalised with **1**. In contrast to prior time-consuming multistep synthesis of dyadic porphyrin photosensitiser (PS) and Re-based catalyst assemblies (*e.g.*, via alkyl chains, phenyl spacers, or amide group), here, interfacing was achieved in mild conditions through supramolecular Zn–N interactions.[24–28] We took advantage of the penta-coordination preference of zinc in porphyrins and the strong affinity of azoarenes for Zn porphyrins to form a self-assembled dyadic system confined inside the porous network.[29] Reminiscent of the Mg chlorophylls held by axial ligation of histidine on the

natural light harvesting antennae protein scaffold, this approach enables the introduction of matching dyadic systems into two different MOF topologies towards monitoring the topology-catalysis relationships. Applying these Re-PCN colloids for photocatalytic CO_2 reduction in acetonitrile (MeCN) with a SED showed a 9-fold TON_{CO} enhancement for PCN-222 over PCN-224 hybrids as well as a 10-fold increase compared to the homogeneous catalyst-porphyrin dyad. Characterisations by powder X-ray diffraction (PXRD), solution and solid-state UV-vis, and attenuated total reflectance infrared (ATR-IR) spectroscopy; inductively coupled plasma mass spectrometry (ICP-MS); N_2 adsorption; density functional theory (DFT) calculations and difference envelope density (DED) analysis uncovered mechanistic insights controlling reaction rate (via topology-guided mass and exciton transport) and selectivity (via wavelength-enabled electron/energy channel switching).

Results and discussion

Synthesis and characterisation

The quaterpyridine ligand and *fac*-$ReBr(CO)_3(qtpy)$ (**1**) were synthesised following literature known procedures,[30,31] while the linker 5,10,15,20-tetrakis(4-carboxyphenyl)porphyrin (**2**) was prepared by saponification of 5,10,15,20-tetrakis(4-methoxycarbonylphenyl)-porphyrin (TPPCOOMe), attained from pyrrole and methyl 4-formylbenzoate.[32] The Zn-metalated analogue of **2** (**2-Zn**) was prepared by reacting TPPCOOMe with $ZnCl_2$, followed by saponification (details in the ESI) for

benchmarking purposes. PCN-222 (**222**) and PCN-224 (**224**) syntheses were adapted from literature and the as-synthesised MOFs were treated with HCl in *N,N*-dimethylformamide (DMF) at 120 °C for modulator removal.[14,33] Zinc metalation of the free base porphyrin linkers was performed in DMF at 100 °C for 24 h resulting in PCN-222(Zn) (**222-Zn**) and PCN-224(Zn) (**224-Zn**) (details and characterisation available in ESI†).[34,35]

1 was integrated into **222-Zn** and **224-Zn**, respectively, by soaking the MOFs in a 0.1 mM stock solution of **1** in MeCN resulting in **1**@PCN-222(Zn) (**Re-222**) and **1**@PCN-224(Zn) (**Re-224**), respectively, and isolated as powders. Loading of **1** was monitored by UV-vis measurements of the supernatant which displayed a strong decline in the intensity of the absorption bands of **1** after 24 h (Fig. S1†). After washing the composites with MeCN, no absorption bands of the catalyst were visible in the UV-vis spectrum of the washing solution, excluding strong leaching of the catalyst and underscoring robust Zn–N interactions (Fig. S2†). Control experiments performed by soaking the Zn-free MOF **222** or **224** in a 0.1 mM solution of **1** showed no decrease in supernatant absorption, confirming the specific dyadic anchoring site of **1** at Zn centres (Fig. S3†).

The unaltered PXRD data of both MOFs upon Zn metalation and Re catalyst incorporation revealed preserved phase purity and crystallinity while being in accordance with the simulated patterns (Fig. 2a). The ATR-IR spectra of both **Re-222** and **Re-224** display symmetric and asymmetric CO vibrations at 1926 and 2025 cm^{-1} and 1927 and 2024 cm^{-1}, respectively (Fig. 2b and S4†), characteristic of **1**, and suggesting successful entrapment as well as unaffected molecular structure after immobilisation in the MOFs.[36] Furthermore, the shift of Zn–N bands at ~398 cm^{-1} after loading of **1** hints at a comprehensive coordination of the Zn porphyrins (Fig. S5†).[37]

Solid-state UV-vis spectra showed comprehensive absorption in the visible-light region for both metalated MOFs, highlighting the suitability of these materials for broad range visible light harvesting (Fig. S6 and S7†). While **222** and **224** display broadened absorption features in line with **2**'s characteristic Soret band at 420 nm and the Q-bands in the range of 510–650 nm (Fig. S8†), hallmark symmetry-restoring changes were observed upon Zn metalation potentially indicating quantitative Zn metalation. In contrast, incorporation of **1** does not affect the absorption spectra suggesting that visible light irradiation will mainly result in MOF host excitation (Fig. S1, S6 and S7†).

ICP-MS performed after MOF digestion of **222-Zn** and **224-Zn** revealed Zr : Zn ratios of 1.8 and 1.9, respectively, indicating that every porphyrin is likely metalated (as Zr : Zn$_{theoretical}$ = 3 and 4, respectively, assuming reaction yield = 100%) and that additional Zn is physisorbed in the MOF pores (Table S1†). Together with the Zn-TCPP, these may act as additional anchoring sites for **1**. Nevertheless, the Re content in **Re-222** and **Re-224** was found similar, ~82 and ~75 nmol$_{Re}$ mg$_{MOF}$$^{-1}$, respectively, further confirming the successful incorporation of **1** in **222-Zn** and **224-Zn** (~0.1 catalyst per linker in both cases, see Table S1†). Loading values are comparable to other molecule-MOF hybrids which often use carboxylic or phosphonic acids for node- or linker-anchoring.[9,12,19,38] Accordingly, our approach provides a synthetically straightforward alternative anchoring design to traditional acid groups (increasing the design space and assembly flexibility) while still affording stable tethering and similar loadings.

Nitrogen adsorption measurements showed a reduction in the N$_2$ quantity adsorbed for both **222-Zn** and **224-Zn** compared to the corresponding pristine MOFs. The Brunauer–Emmett–Teller (BET) surface area was reduced from ~1990 to ~1550 m^2 g^{-1} for **222** and **222-Zn**, and from ~1980 to ~1750 m^2 g^{-1} for **224** and **224-Zn**, respectively (Fig. S9 and S10†). Such a decrease upon metalation is common and has been observed for other PCN analogues.[8,34] A further decrease of the N$_2$ quantity adsorbed upon incorporating **1** is observable for both MOF topologies (Fig. 2c and S10†). The N$_2$ quantity adsorbed in **Re-224** is more dramatically reduced compared to **Re-222**, indicating a higher extent of pore blocking in the former case. This is further illustrated by the BET surface areas and calculated pore size distributions of ~1219 m^2 g^{-1} for **Re-222**, while a BET surface area of merely ~618 m^2 g^{-1} is obtained for **Re-224**. Scanning electron microscopy (SEM) images visualised rod-shaped ~10 × 1 μm **222** crystals and cube-type ~0.5 × 0.5 μm **224** crystals, in line with literature (Fig. S11 and S12†).[14]

Previous studies have reported on the measurements of conduction and valence band levels of PCN MOFs.[39] Alternatively, a recent study on a PCN-molecular catalyst hybrid showed
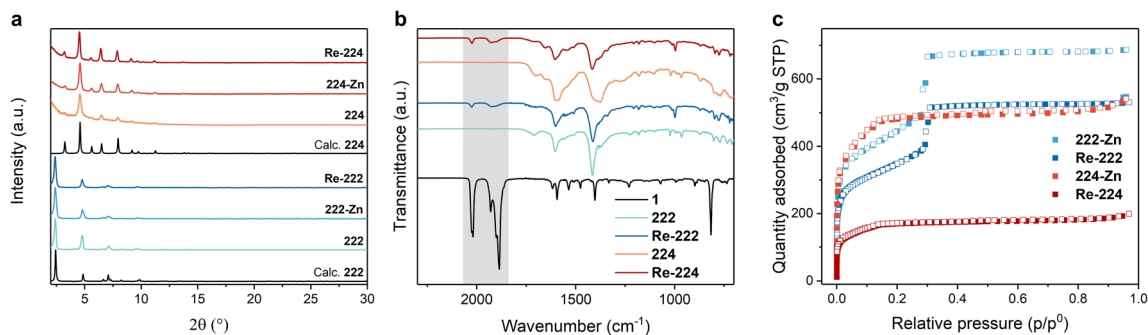

Fig. 2 Material characterisation for pristine and loaded PCN-222 and PCN-224 assemblies. (a) Measured PXRD data. (b) ATR-IR spectra including the reference for pure catalyst **1** (black trace) and with the characteristic region for Re(CO)$_3$ bands highlighted in grey. Full spectra in ESI.† (c) N$_2$ sorption isotherms at 77 K.

that complete isolation of the organic porphyrin linkers in a rigid structure with insulating metal nodes prevents an electronic coupling, concluding that excited energy levels of PCN MOFs can be regarded as those of the free linker.[19] The oxidation potential of **2-Zn*** (S_1) was previously calculated at -1.24 V vs. saturated calomel electrode (V_{SCE}).[19] With $E(1/1^-) = -0.64$ V_{SCE}, photoinduced electron transfer from **2-Zn*** to **1** in the PCN assemblies is thermodynamically possible, and was reported as the preferred first electron transfer step for Re-porphyrin dyads, as opposed to reductive quenching by the SED.[24,25,31] In photocatalysis conditions, the corresponding oxidised PS at $E = 0.88$ V_{SCE} will react with 1,3-dimethyl-2-phenyl-2,3-dihydro-1*H*-benzo[*d*]imidazole (BIH) employed as a benign SED to regenerate the PS ground state with $E(BIH^+/BIH) = 0.33$ V_{SCE} (Fig. S13†).[39,40]

In summary, assembly characterisation suggests similar catalyst loading and light-absorbing behaviour for both topologies, however, differing in permanent porosity and, accordingly, likely differing in substrate-catalyst accessibility.

Photocatalysis under broadband irradiation

Photocatalysis experiments were conducted under heterogeneous colloidal conditions, namely suspended MOF assembly (1.5 mg) in wet organic media (4 mL MeCN and 0.12 mL deionised H_2O) and BIH (225 mg, 1 mmol) as the SED. The resulting suspension was saturated by bubbling CO_2. Irradiation was performed with a Xenon Light Source (300 W, $\lambda = 430$–740 nm, $\sim$10 mW cm^{-2}). CO and H_2 evolution were analysed by gas chromatography of the reaction headspace, while formate formation was investigated by ^1H NMR of the reaction solution.

First, we examined the activity of the homogeneous dyadic PS-catalyst system as a benchmark for the Re-PCN assemblies towards CO_2 reduction. To verify the dyadic system in solution, UV-vis spectra of 0.05 mM **2-Zn** in MeCN before and after the addition of equimolar quantities of **1** were recorded (Fig. S14†). These displayed a 5 nm bathochromic shift of the Soret band from 414 to 419 nm indicating self-assembly of **1** and **2-Zn** in solution.[41]

As $ReX(CO)_3(bpy)$-based catalysts can photoreduce CO_2 without an external photosensitiser,[22,42] irradiation of **1** in the catalytic media (identical to heterogeneous conditions above) gave selective CO formation with a maximal TON$_{CO}$ of $\sim$5 after 2 h. Repeating the experiments in presence of an equimolar amount of **2-Zn** yielded TON$_{CO}$ $\sim$10 (Fig. 3a and Table S2, see ESI† for TON calculation). While low stability under photocatalytic conditions is a common issue of Re catalysts, such a low activity compared to other reports on $ReX(CO)_3(bpy)$-based catalysts and porphyrin–rhenium-catalyst dyads (with TONs in the low 100s) highlights the influence of the (pyridine) linking units.[22,26–28,43]

Remarkably, irradiating **Re-222** colloids in photocatalytic media for 80 h conversely produced $\sim$27 μmol_{HCOO^-} g^{-1} h^{-1} (TON$_{HCOO^-}$ per node $\sim$5) and subcatalytic amounts of CO ($\sim$4 μmol_{CO} g^{-1} h^{-1}; TON$_{CO}$ per Re < 1) (Fig. 3a, b, Tables S3 and S4†). Incident photon conversion efficiency measurements and apparent quantum yield (AQY) calculations (details in ESI, Tables S5 and S6†) gave values of $\sim$0.01% (CO) and $\sim$0.10% (formate) at
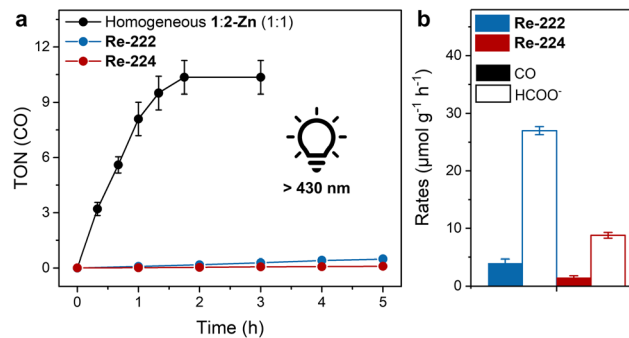

Fig. 3 Photocatalytic CO_2 reduction performance. (a) TON(CO) vs. time plot for MOF samples, including the homogeneous reference (black trace). (b) Product evolution rates averaged over the first two irradiation hours. Standard conditions: MOF sample (1.5 mg) suspended in MeCN (4 mL) and deionised H_2O (0.12 mL) with BIH (225 mg), room temperature, continuous >430 nm irradiation.

$\lambda = 450$ nm. AQYs in the range of 0.1–3.0% are common for colloidal visible light-driven CO_2 reduction for comparable systems.[19,44,45] Control photocatalysis experiments using Re-free **222-Zn** showed no CO evolution but a comparable formate production rate, while experiments run without BIH or light yielded in all cases no detectable CO, H_2 or formate (Table S3†). Product generation can be ascribed to light absorption by **2** followed by electron transfers to the CO-selective Re catalysts or to the Zr-oxo node-catalysts for formate production. The latter is in line with previous reports, and suggest two competing CO_2 reduction mechanisms concomitantly occurring in **Re-222**.[17,18,39,46] The corresponding **Re-224**-based experiments showed overall lower TONs and rates than for **Re-222** but similar reactivity trends favouring formate over CO production, i.e., $\sim$2 μmol_{CO} g^{-1} h^{-1} and $\sim$9 μmol_{HCOO^-} g^{-1} h^{-1} (Fig. 3a, b and Table S3†).

While interfacing the Re catalyst amid the MOF significantly increases its lifetime compared to when employed in homogenous conditions, its catalytic involvement is limited as formate evolution prevails. Together with impeded CO evolution, differing numerical performance between the two hybrid MOFs underlines a key influence of the host on the photocatalytic activity.

Post-catalysis PXRD analysis of **Re-222** and **Re-224** showed crystalline frameworks, while the $Re(CO)_3$ moiety was no longer visible in the corresponding ATR-IR spectrum (Fig. S15 and S16†). This suggests that while the host is virtually stable under catalysis conditions, the catalyst is not, in line with its homogeneous instability.[9,43,47]

To examine the reasons for the differing product evolution rates in **Re-222** and **Re-224** samples, as well as the dramatic change of product selectivity between homogeneous and heterogeneous systems, the photocatalytic mechanism was investigated through spectroscopic and catalytic experiments.

Catalytic mechanism investigation and photocatalysis under selective irradiation

The topology of PCN-222 and -224 differs significantly. While **222** has hexagonal channels of $\sim$35 Å in size and trigonal
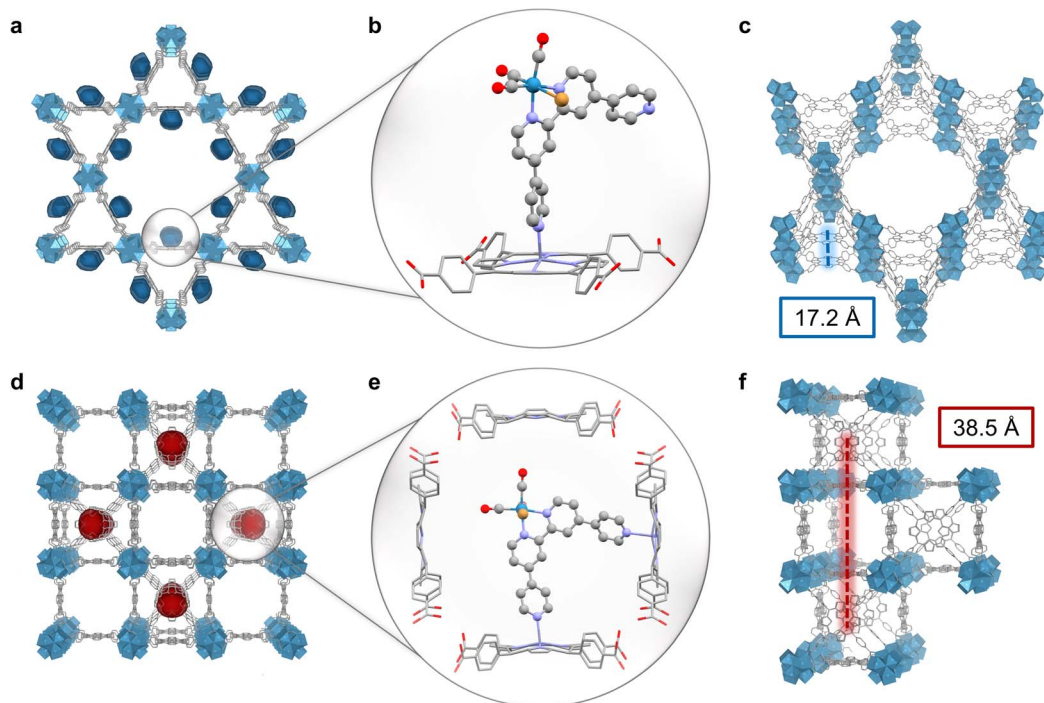
Fig. 4 (a) DED map for **Re-222**. (b) DFT-optimised dyad of **1** and **2-Zn** in **222**'s pore fragment. Red: oxygen, grey: carbon, purple: N, gold: Br, cyan: Re. H atoms omitted for clarity. (c) Translational exciton hopping distance in **222**-based assemblies. (d) DED map for **Re-224**. (e) DFT-optimised dyad of **1** and **2-Zn** in **224**'s pore fragment. (f) Translational exciton hopping distance in **224**-based assemblies.

channels of ~10 Å, **224** has cubic pores/impeded channels with ~20 Å diameter (Fig. 1c and S10†).[8,13] The geometric structure of the catalyst optimised by DFT calculations yielded a maximum van-der-Waals sphere diameter of ~13.5 Å, smaller than the MOFs' pore apertures (Fig. 1b, atomic coordinates in ESI†). Despite similar molecular loadings of **1**, partial pore blocking is likely more prominent in **Re-224** than **Re-222** as shown by the former's lower N_2 uptake (Fig. 2c and Table S1†). DED analysis was thus performed to map the electron density introduced by **1**. Briefly, measured PXRD patterns were Le Bail-refined and the resulting structure factors were used to create structure envelopes for pristine and loaded MOFs, which were subtracted from each other (Fig. S17–S20, details in ESI†).[48] For **Re-222**, **1** was found directed into the hexagonal channels leaving inner space for substrate diffusion (Fig. 4). In contrast, for **Re-224**, **1** fills almost the complete space of every second pore. These observations are supported by DFT calculations of **1** in a pore fragment of each MOF, confirming the catalyst positions suggested by DED analysis (Fig. 4a, b, d and e; details and atomic coordinates in ESI†). Specifically, for **Re-224**, this implies pore blocking potentially further rationalised by DFT calculations that also revealed the possibility of anchoring **1** via two coordinating N–Zn bonds to neighbouring Zn-porphyrins in **Re-224**. Together with ATR-IR spectra (shift of Zn–N bands after **1** loading), steric pore restrictions (particularly for **224-Zn**), and comparable catalyst loadings per linker for **Re-222/Re-224**, the DED analysis supports that anchoring of **1** occurs predominantly at the TCPP-bound Zn (Fig. 4, S5 and Table S1†). While not directly observed, partial coordination to physisorbed Zn cannot be ruled out.

Overall, these analyses depict a more hindered nano-environment in **Re-224** than in **Re-222** potentially limiting reactant (e.g., BIH max. diameter = 10.6 Å),[21] and product diffusion in line with a lower catalytic activity for the former.

Besides mass transport, transferring conclusions from recent reports on MOF-based exciton migration suggest that charge separation (CS) probability is significantly favoured for **Re-222** over **Re-224**, due to topology-induced higher exciton hopping rates and a lower Förster radius R between chromophores (Förster resonance energy transfer scaling with R^{-6}).[20,49] Here, the translational hopping distance along the c-axis is ~17 Å for **222**, and ~39 Å for **224** (Fig. 4c and f and non-translational distances in Fig. S21†). Additionally, **222**'s triangular motif with cofacial conformation translating along the lateral direction of the crystallographic c-axis further improves excited state delocalisation and hopping rates,[50] due to head-to-tail coupling.[51]

Steady-state luminescence measurements were conducted towards further understanding of photoinduced processes in our systems. Luminescence experiments on a 0.05 mM solution of **2-Zn** in MeCN showed two prominent emission bands at $\lambda =$ 649 and 714 nm upon excitation at either 415 or 515 nm (Soret or Q band, respectively) (Fig. 5a and b), matching literature reports ascribed to the de-excitation of the S_1 states.[52] The latter is produced by: internal conversion of the S_2 state, via Soret region irradiation, or directly, via Q-band irradiation. Adding an equimolar amount of **1** to the solution to replicate homogeneous catalysis system resulted in a quenching of the luminescence intensity, comparable for both excitation wavelengths, and ascribed to photoinduced intramolecular electron transfers
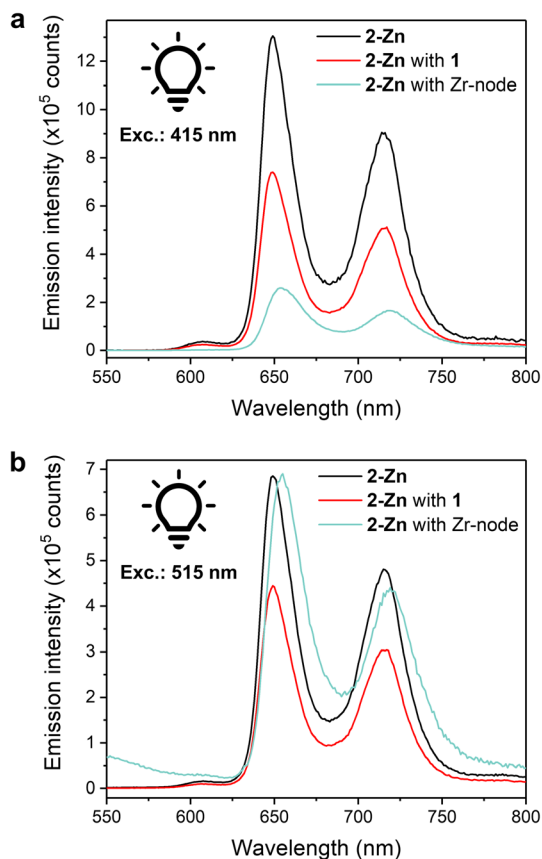
Fig. 5 Liquid-phase fluorescence spectra of MeCN/DMF (40/1 v/v) solutions containing **2-Zn** (0.05 mM), **2-Zn** (0.05 mM) and **1** (0.05 mM), and **2-Zn** (0.05 mM) with the isolated Zr$_6$-oxo-node (0.2 mM). (a) Excitation at 415 nm. (b) Excitation at 515 nm.

from **2-Zn** to **1**. Incomplete quenching possibly stems from dynamic self-assembly and unpaired **2-Zn** as well as inefficient electron transfer. With fluorescence experiments on colloid MOFs being challenging due to high scattering and sedimentation propensity, fully soluble Zr-oxo-based assemblies were prepared as small-scale counterparts of the hybrid PCN systems to enable properties replication and photophysical investigations. Discrete Zr$_6$-oxo-nodes (Zr$_6$), featuring methacrylate ligands as capping agents to prevent aggregation, were synthesised and isolated following a literature procedure (see ESI†).[53] Associating these with **2-Zn** yielded the fully soluble CO$_2$H-tethered composites Zr$_6$|**2-Zn** (see ESI† for assembly conditions) and allowed solution fluorescence measurements without affecting **2-Zn**'s absorption properties (Fig. S22†). In stark contrast to the Zr$_6$-free homogeneous systems, a lower luminescence intensity was recorded after excitation at 415 nm (Fig. 5a) whereas excitation at 515 nm afforded a spectrum comparable to the one of **2-Zn** (Fig. 5b). These behaviours were also reproduced in the corresponding action spectra (λ_{em} = 720 nm) as Zr$_6$|**2-Zn** displayed unchanged Q-band contributions compared to **2-Zn**, and adding **1** resulted in lesser contributions (Fig. S23†).

Such wavelength-dependent luminescence behaviour hints at different energy relaxation pathways. Here, excitation into the

Soret band in the Zr$_6$|**2-Zn** assembly results in a high-energy S$_2$ state (zero–zero transition energy, $E_{00} \approx$ 2.9 eV) and likely induces fast electron transfer to a Zr-oxo cluster.[18] As no fluorescence quenching was observed upon Q-band irradiation, this pathway is disabled from the S$_1$ state possibly due to its lower energy level ($E_{00} \approx$ 2.0 eV). This also implies that the kinetics of charge separation from S$_2$ are significantly faster than the S$_2 \rightarrow$ S$_1$ internal conversion. While Zn porphyrins present various and complex relaxation mechanisms, this interpretation is coherent with the documented slow S$_2 \rightarrow$ S$_1$ kinetics in Zn porphyrins, and in line with hot electron transfers from S$_2$ as previously observed in molecular dyads and in heterogeneous assemblies.[25,54,55] As inferred by the wavelength-independent quenching of fluorescence in the **2-Zn** with **1** system (Fig. 5), reduction of **1** from the S$_1$ excited state of **2-Zn** is anticipated and consistent with the significant associated exergonicity (change in Gibbs free energy value, ΔG_{CS} = −0.6 eV).

To investigate whether this behaviour is reflected in the photocatalysis performance, we performed a series of wavelength-dependent investigations using lower energy-centred wavelengths λ = 490–740 nm (~8 mW cm^{-2}), thus omitting Soret band excitation and corresponding S$_2$ excited state production.

For **Re-222**-based experiments, a dramatically increased reactivity, and a reversed selectivity from HCOO$^-$ to CO were observed with ~370 μmol$_{CO}$ g^{-1} h^{-1} and <1 μmol$_{HCOO^-}$ g^{-1} h^{-1} (Fig. 6a and Table S3†). Correspondingly, TON$_{CO}$ ~100 were reached after 80 h compared to below 1 obtained with λ > 430 nm and a higher absolute light intensity (Fig. 3a, 6b, Tables S3 and S4†). **Re-224**-based experiments gave a similar trend with ~24 μmol$_{CO}$ g^{-1} h^{-1} (TONs$_{CO}$ ~ 12) and <1 μmol$_{HCOO^-}$ g^{-1} h^{-1} after ~60 h, albeit with the absolute performance remaining significantly inferior to **Re-222** due to its topological limitations (Fig. 6a, b and Table S3†). With selective irradiation predominantly yielding formate or CO (Table S3†), electronic communication between nodes and Re catalysts within the pores is unlikely. After 80 h of >490 nm irradiation PXRD analysis of **Re-222** and **Re-224** showed crystalline framework retention, while the Re(CO)$_3$ moiety was no longer visible in ATR-IR spectra, comparable to >430 nm irradiation (Fig. S15 and S16†). For **Re-222** and **Re-224**, post-catalysis ICP-MS measurements revealed that 27 and 17% of immobilised Re leached into the supernatant, respectively (Table S7†). This is consistent with other reported photodegradations of Re catalysts and described complex decomposition and subsequent loss of activity.[9,43,47,56] In addition, corresponding dynamic light scattering measurements revealed no Re nanoparticle formation (Fig. S24†).

Control experiments with ^{13}C-labelled CO$_2$ for both Re-PCN hybrids produced only [13]CO, confirming that CO$_2$ was the sole source of CO (Fig. S25†). Further control experiments conducted with the CO$_2$H–analogue of **1**, i.e., fac-ReBr(CO)$_3$(4,4′-dicarboxy-2,2′-bipyridine), node-anchored in PCN-222 and PCN-224 (synthesis in ESI, Fig. S26–S28 and Table S1†) showed comparable wavelength-dependent performance trends to **Re-222** and **Re-224** under identical reaction conditions (Table S3†). This is consistent with a previously reported PCN-222-Re assembly displaying selective CO$_2$-to-CO evolution upon
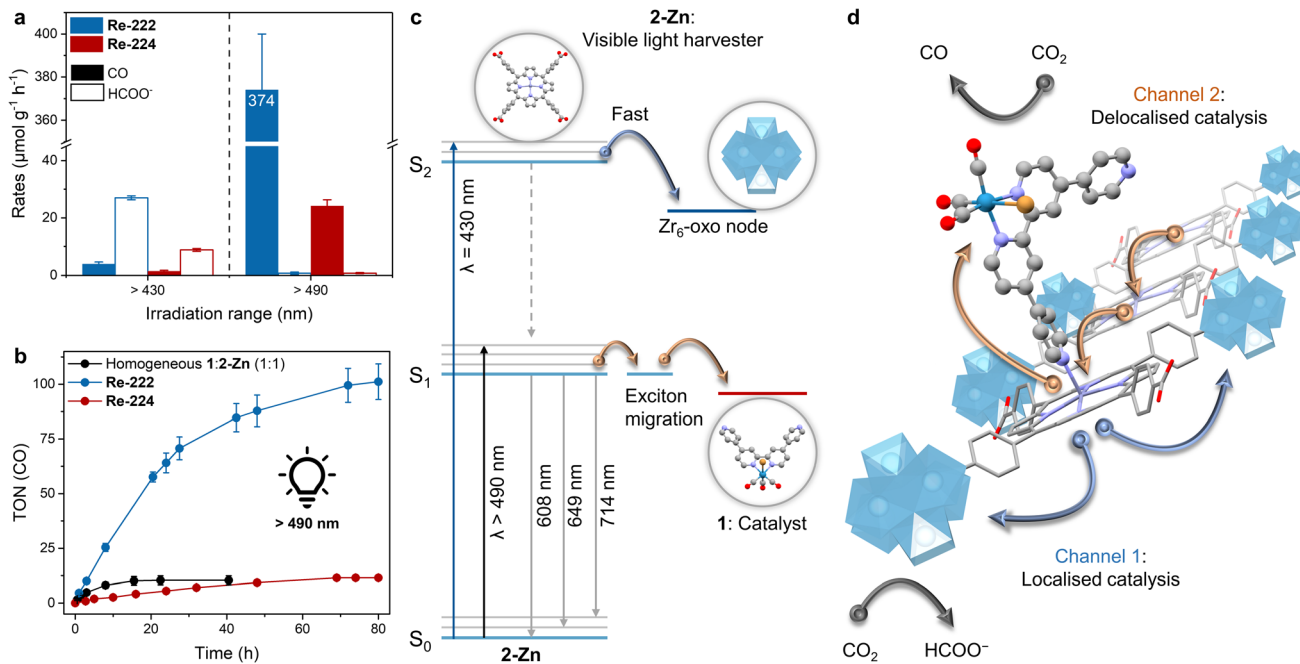
Fig. 6 Wavelength-dependent photocatalytic CO_2 reduction with Re-PCN assemblies. (a) Product evolution rates depending on irradiation wavelength averaged over the first two irradiation hours. (b) TON(CO) *vs.* time plot for MOF samples irradiated >490 nm. Includes the homogeneous reference (black trace). Standard conditions are MOF sample (1.5 mg) suspended in MeCN (4 mL) and deionised H_2O (0.12 mL) with BIH (225 mg), room temperature, continuous irradiation. (c) Schematic energy level diagram illustrating the working principle upon irradiation at different wavelengths. (d) Schematic representation of the two irradiation wavelength–dependent electron channels observed in Re-PCN hybrids to either deliver localised electrons to the node for CO_2-to-formate, or delocalised exciton migration followed by charge separation to the molecular catalyst for CO_2-to-CO. Note that for reasons of clarity not all nodes are shown.

>500 nm irradiation[19] and thus excludes the catalyst and dyadic motif as the source of the observed trends.

These wavelength-dependent results suggest that excited state (S_2 *vs.* S_1)-specific, selectivity-dictating catalytic channels are occurring in the MOF assemblies, with electron delivery to the CO evolution molecular catalyst or the formate producing node being selectively activated by low or high energy wavelength, respectively. This was confirmed by AQY measurements at $\lambda = 520$ nm, giving ~0.35% (CO) and ~0.01% (formate), showing a reverse trend compared to 450 nm values (Tables S5 and S6†).

Interestingly, the correlations between product selectivity and irradiation wavelength were found in both Re-PCN assemblies as well as in the homogeneous $Zr_6|$**2-Zn**$|$**1** system. The latter showed limited CO evolution (TONs ~ 1) and traces of formate using full irradiation, while >490 nm irradiation experiments yielded TONs ~10 (Table S2†). By contrast, homogeneous Zr_6-free molecular **2-Zn** with **1** delivered wavelength-independent performance. This further highlights the critical impact of the assembly/framework (MOF *vs.* molecular assemblies) on photocatalysis (Fig. 3a, b, 6a, b, Tables S2 and S3†).

Luminescence and catalytic experiments together provide consistent evidence that irradiation with $\lambda > 430$ nm during photocatalysis mainly results in excitation of the Soret-band (S_0–S_2 transition, Fig. S6–S8†) in PCN assemblies upon which the S_2 state is rapidly quenched by electron transfer to the Zr_6-oxo-node (Fig. 6c).[17,18,39] Here, bimolecular reaction with the diffusing SED is likely to proceed subsequently to regenerate the ground state (Fig. S13†) or detrimental charge recombination occurs.[19] Selective CO_2-to-formate reduction proceeds *via* reduced Zr(III) centres upon collecting another electron.[17,46] With each linker connected to four nodes and charge separation occurring at the light harvesting centre, this constitutes a localised electron channel (Fig. 6d). Shifting to irradiation with $\lambda > 490$ nm mainly results in excitation of the Q bands (S_0–S_1 transition),[55] affording a lower energy excited state unable to trigger node-quenching but able to reduce **1**. The latter effects selective CO_2-to-CO reduction upon accumulating two electrons.[9,19] Alternatively, in absence of a Re catalyst in direct vicinity, directional exciton migration proceeds within the MOF structure.[19] As an exciton can visit 100+ linkers in its lifetime,[19,51] this energy funnelling is highly delocalised and provides a long-range, antennae-like catalytic channel (Fig. 6d).

The minute, deactivated CO evolution when using full irradiation is noteworthy considering that Soret and Q bands are concomitantly excited. The rationale is likely intricated and may involve substrate diffusion, competing photophysical processes and slower CO catalysis kinetics. Tentatively, the high molar absorption of S_2 together with an excess of nodes to catalysts (statistically each linker neighbours four Zr_6 nodes and ~0.1 Re catalysts, Table S1†) could result in a kinetic preference for available CO_2 (with affinity to coordinate to Lewis-acidic Zr nodes) to be converted to formate, depleting local substrate

concentrations.[57] While future in-depth spectroscopic studies are needed to elucidate this phenomenon, this finding may hold important repercussions as most literature research focuses on full spectrum broadband irradiation.

Overall, the results show that the linker's excited states and quenching kinetics with the molecular catalyst *vs.* the node are critical for understanding and tailoring reactivity. As a perspective, the observed wavelength-dependency provides an edge over similar systems as these usually show a reverse trend, *i.e.*, high-energy (near) UV irradiation achieves higher performance.[45,58] Here, lower-energy visible light provides selective molecular CO_2-to-CO reduction, allowing unusual control over product selectivity based on irradiation wavelength.

Experimental

For a comprehensive description of analytical methods and experimental procedures the reader is referred to the ESI.† An overview of the central syntheses is provided here.

Synthetic procedures

4,4′:2′,2″:4″,4‴-Quarterpyridine (qtpy). The synthesis was adapted from a literature known procedure.[30] 4,4′-Bipyridine (2.50 g, 16.0 mmol) and 0.50 g Pd/C (10 wt%) were heated in a Teflon bomb at 250 °C for 48 h. The resulting solid was ground and Soxhlet extracted with dichloromethane (DCM, 300 mL) over 18 h, giving a first fraction. The Pd residue was washed with hot DMF (2 × 50 mL), giving a second fraction. The solvents of both fractions were removed, the residues were combined, and purified by flash column chromatography (DCM/MeOH 91/9 v/v) and subsequently *via* sublimation to yield the pure product (0.77 g, 31%), whose characterisations matched literature reports (see ESI†).

***fac*-ReBr(CO)₃(qtpy) (1).** The synthesis was adapted from a literature known procedure.[31] ReBr(CO)₅ (140 mg, 0.35 mmol, 1.00 eq.) was dissolved in a mixture of dry and degassed toluene/THF (25 mL, 3/1 v/v) under Schlenk conditions. Subsequently, 4,4′:2′,2″:4″,4‴-quarterpyridine (112 mg, 0.36 mmol, 1.05 eq.) was added. The yellow solution was refluxed for 24 h. After cooling, an orange solid precipitated. The suspension was filtered and the residue washed with CHCl₃ (2 mL). The solid was dried *in vacuo* to give the pure product as an orange powder (144 mg, 63%), whose characterisations matched literature reports (see ESI†).

5,10,15,20-Tetrakis(4-carboxylphenyl)-porphyrin (2). The synthesis was adapted from a literature known procedure.[32] The first step was the synthesis of 5,10,15,20-tetrakis(4-methoxycarbonylphenyl)-porphyrin (TPPCOOMe) by adding pyrrole (3.09 mL, 44.9 mmol, 1.1 eq.) and methyl-*p*-formylbenzoate (6.93 g, 42.3 mmol, 1.0 eq.) to refluxing propionic acid (100 mL). After refluxing for 22 h under continuous stirring, the precipitate was filtrated and washed with MeOH (30 mL), EtOAc (10 mL) and THF (10 mL) to yield the purple product (5.45 g, 6.44 mmol, 15% yield), whose characterisations matched literature reports (see ESI†). In the second step, TPPCOOMe (1.00 g, 1.19 mmol, 1.0 eq.) was dissolved in a 1 : 1

mixture of THF/MeOH (70 mL). A solution of KOH (3.5 g, 62.4 mmol, 52 eq.) in H₂O (30 mL) was added. The resulting mixture was refluxed for 15 h. After removing the organic solvents *in vacuo*, the solid was redissolved in H₂O (150 mL) at 90 °C for 15 min. The solution was filtered and acidified with 1 M HCl (100 mL). The resulting green precipitate was filtered and dried to obtain the product (864 mg, 1.09 mmol, 92% yield), whose characterisations matched literature reports (see ESI†).

5,10,15,20-Tetrakis(4-carboxylphenyl)-porphyrin-Zn(ɪɪ) (2-Zn). TPPCOOMe (854 mg, 1.01 mmol, 1.0 eq.) and ZnCl₂ (1.75 g, 12.8 mmol, 12.8 eq.) were refluxed in DMF (100 mL) for 6 h. After the mixture was cooled to room temperature, H₂O (150 mL) was added. The dark purple precipitate was filtered and washed with H₂O (2 × 50 m mL). The obtained solid was dissolved in CHCl₃ (500 mL) and washed with H₂O (3 × 250 mL). The organic layer was dried over anhydrous Na₂SO₄. Subsequently, the solvent was removed by rotary evaporation to yield TPPCOOMe-Zn(ɪɪ) (276 mg, 303 μmol, 30% yield, see ESI†).

This intermediate (214 mg, 235 μmol, 1.0 eq.) was dissolved in THF/MeOH 1 : 1 (15 mL). KOH (691 mg, 12.3 mmol, 52 eq.) was dissolved in H₂O (6 mL) and added to the prior solution. The reaction mixture was refluxed for 5 h under continuous stirring. After the mixture was cooled to room temperature, the organic solvents were removed by rotary evaporation. The crude product was dissolved in H₂O (32 mL) and heated at 90 °C for 10 min. After cooling to room temperature, the aqueous mixture was acidified with 1 M HCl solution (21 mL) and 37% HCl (1 mL) in respective order. The resulting dark green precipitate was isolated by centrifugation and washed with H₂O (8 × 30 mL). The dark green product was dried *in vacuo* overnight (137 mg, 161 μmol, 68% yield, see ESI†).

PCN-222. The synthesis was adapted from a literature known procedure.[14,33] In a 20 mL screw cap vial, 2 (12.5 mg, 0.016 mmol, 1.00 eq.) and ZrOCl₂·8H₂O (23.5 mg, 0.073 mmol, 4.56 eq.) were dissolved in *N,N*-diethylformamide (DEF, 3 mL). After addition of 4-*tert*-butylbenzoic acid (1350 mg, 7.57 mmol, 473 eq.), the mixture was ultrasonicated for 10 min. The mixture was heated at 120 °C for 12 h in an oven. The solid was separated by centrifugation and soaked with DMF (3 × 6 mL) and dried *in vacuo*. The solid (12.2 mg) was dispersed in DMF (8.1 mL) and acidified with 8 M HCl (0.3 mL). The mixture was heated in an oven at 120 °C for 12 h. The purple solid was collected by centrifugation and soaked in DMF (3 × 6 mL) and acetone (3 × 6 mL) and dried *in vacuo* to yield the product, whose characterisations matched literature reports (see ESI†).

PCN-224. The synthesis was adapted from a literature known procedure.[14,33] In a 20 mL screw cap vial, 2 (16.0 mg, 0.020 mmol, 1.00 eq.) and ZrOCl₂·8H₂O (30.0 mg, 0.093 mmol, 4.65 eq.) were dissolved in DMF (4 mL). After addition of formic acid (0.69 mL, 17.2 mmol, 860 eq.) and 3,3-dimethylbutanoic acid (0.81 mL, 6.36 mmol, 318 eq.), the mixture was ultrasonicated for 10 min. The mixture was heated at 120 °C for 12 h in an oven. The solid was separated by centrifugation and soaked with DMF (3 × 6 mL) and dried *in vacuo*. The solid (31.1 mg) was dispersed in DMF (21 mL) and acidified with 8 M HCl (1.6 mL). The mixture was heated in an oven at 120 °C for 12 h. The purple solid was collected by centrifugation and soaked in

DMF (3×10 mL) and acetone (3×10 mL) and dried *in vacuo* to yield the product, whose characterisations matched literature reports (see ESI†).

Metalation of 222 or 224 with Zn. The synthesis was adapted from a literature known procedure.[34,35] ZnCl$_2$ (59.9 mg for **222** and 22.9 mg for **224**) was dissolved in DMF (3 mL). After addition of the MOF powder (30 mg), the suspension was heated in an oven at 100 °C for 24 °C. The product was isolated by centrifugation and washed with DMF (3×6 mL) and acetone (3×6 mL). Drying *in vacuo* yielded the product, whose characterisations matched literature reports (see ESI†).

Molecular catalyst loading in 222-Zn or 224-Zn. A 0.1 mM solution of **1** in MeCN (15 mL) was added to powder samples of the respective activated MOF sample (10.0 mg) in VWR® TraceClean® 20 mL vials. After 24 h in the dark, the suspension was centrifuged, and the supernatant removed. The resulting powder was washed with fresh MeCN (3×7 mL) for 2 h per wash cycle and then dried overnight *in vacuo*.

Photocatalytic CO$_2$ reduction. Photocatalytic tests were performed in air-tight 50 mL Schlenk flasks with the respective MOF material (1.5 mg), a stir bar, MeCN (4 mL), deionised H$_2$O (0.12 mL, 3 vol%) and BIH (225 mg, 1 mmol). For CO$_2$ reduction the reaction suspension and headspace were fully saturated with CO$_2$ for seven minutes and after sealing a CO$_2$ overpressure was applied, totalling a pressure of 1.45 bar.

The irradiation source was a heat-free white light generator Asahi Spectra MAX-303 Compact Xenon Light Source 300 W, with either a XVL0430-Longpass 430 nm filter (430–740 nm irradiation, $\sim$10 mW cm^{-2}) or a XVL0490-Longpass 490 nm filter (490–740 nm irradiation, $\sim$8 mW cm^{-2}). Reaction products were determined through headspace analysis by gas chromatography and ^{1}H NMR of the reaction solution.

Conclusions

We successfully synthesised and characterised two different hybrids of *fac*-ReBr(CO)$_3$(qtpy) in porphyrinic MOFs (PCN-222 and PCN-224) by post-synthetic self-assembly, allowing straightforward topology-independent catalyst anchoring. Corresponding smaller scale, molecular and supramolecular assemblies were also prepared for comparison and benchmarking purposes. Here, we demonstrated that material interfacing at various scales, *i.e.*, molecule–molecule (**1** + **2-Zn**), molecule-cluster (**Zr$_6$|2-Zn|1**), and molecule-particle (Re-PCNs) produces composites displaying unique and complex behaviours that are concomitantly reminiscent, diverging and unseen in their individual building blocks.

Mainly, assembling Re catalyst-PCN composites afforded photocatalysts bearing two catalytic channels that are selectively activated by specific incident irradiation wavelengths and thus, ultimately govern the catalysis product selectivity. Shorter wavelengths resulted in localised charge transfers from the excited porphyrin linkers to the Zr$_6$-oxo-nodes, producing formate. Alternatively, lower energy irradiation can be used to activate the CO-selective Re catalysts with exciton migration enabling long-range, delocalised catalysis. By contrast, the

corresponding molecular and supramolecular systems yielded product selective and wavelength-independent catalysis.

While molecule-like localised S$_2$ and S$_1$ states more accurately describe the observed photoinduced processes in Re-PCNs over typical band-like description of MOFs, the hybrids also display material-like properties elusive to molecular species. Thus, a topology effect was shown with the PCN-222 hybrids displaying a higher photocatalytic activity over PCN-224, as small pore sizes hinder mass diffusion and short coupling distances promote antennae-effect. Further the nanoparticular hybrid porous systems enabled a 10-fold increase in CO$_2$ reduction activity compared to their discrete counterparts, ascribed to stabilising pore confinement.

Although preliminary, this work constitutes the seminal investigation of the likely considerable influence of MOF topology on solar fuel production. Future efforts on controlled distances between catalyst and photosensitiser, understanding of underlying photoinduced processes, varied anchor principles, as well as optimised energy and mass transport will allow orthogonal component assembly and minimise energy loss for efficient solar fuel production. Finally, we show that while broadband light is often considered in its entirety in the broader literature, a finer differentiation may be needed to understand complex hybrid materials' behaviour and performance.

Data availability

The source data is available from the corresponding author upon reasonable request.

Author contributions

P. M. Stanley: methodology, validation, formal analysis, investigation, data curation, writing – original draft, visualisation. K. Hemmer: methodology, validation, formal analysis, investigation, data curation, writing – original draft, visualisation. M. Hegelmann: investigation, data curation. A. Schulz: investigation, data curation. M. Park: investigation, data curation. M. Elsner: investigation. M. Cokoja: conceptualisation, writing – review and editing, supervision, resources, project administration. J. Warnan: conceptualisation, writing – review and editing, supervision, resources, project administration.

Conflicts of interest

There are no conflicts to declare.

Acknowledgements

References

1 H. J. Sayre, L. Tian, M. Son, S. M. Hart, X. Liu, D. M. Arias-Rotondo, B. P. Rand, G. S. Schlau-Cohen and G. D. Scholes, *Energy Environ. Sci.*, 2021, **14**, 1402.

2 V. Kumaravel, J. Bartlett and S. C. Pillai, *ACS Energy Lett.*, 2020, **5**, 486.

3 K. E. Dalle, J. Warnan, J. J. Leung, B. Reuillard, I. S. Karmel and E. Reisner, *Chem. Rev.*, 2019, **119**, 2752.

4 A. Bachmeier and F. Armstrong, *Curr. Opin. Chem. Biol.*, 2015, **25**, 141.

5 R. Freund, O. Zaremba, G. Arnauts, R. Ameloot, G. Skorupskii, M. Dincă, A. Bavykina, J. Gascon, A. Ejsmont, J. Goscianska, M. Kalmutzki, U. Lächelt, E. Ploetz, C. S. Diercks and S. Wuttke, *Angew. Chem., Int. Ed.*, 2021, **60**, 23975.

6 (a) H. Furukawa, K. E. Cordova, M. O'Keeffe and O. M. Yaghi, *Science*, 2013, **341**, 1230444; (b) G. A. Leith, C. R. Martin, J. M. Mayers, P. Kittikhunnatham, R. W. Larsen and N. B. Shustova, *Chem. Soc. Rev.*, 2021, **50**, 4382.

7 K. Hemmer, M. Cokoja and R. A. Fischer, *ChemCatChem*, 2021, **13**, 1683.

8 K. Epp, B. Bueken, B. J. Hofmann, M. Cokoja, K. Hemmer, D. Vos and R. A. Fischer, *Catal. Sci. Technol.*, 2019, **9**, 6452.

9 P. M. Stanley, C. Thomas, E. Thyrhaug, A. Urstoeger, M. Schuster, J. Hauer, B. Rieger, J. Warnan and R. A. Fischer, *ACS Catal.*, 2021, **11**, 871.

10 X. Feng, Y. Pi, Y. Song, C. Brzezinski, Z. Xu, Z. Li and W. Lin, *J. Am. Chem. Soc.*, 2020, **142**, 690.

11 (a) J. Lyu, X. Zhang, K. Otake, X. Wang, P. Li, Z. Li, Z. Chen, Y. Zhang, M. C. Wasson, Y. Yang, P. Bai, X. Guo, T. Islamoglu and O. K. Farha, *Chem. Sci.*, 2019, **10**, 1186; (b) T.-Y. Zhou, B. Auer, S. J. Lee and S. G. Telfer, *J. Am. Chem. Soc.*, 2019, **141**, 1577; (c) Y. Wang, H. Cui, Z.-W. Wei, H.-P. Wang, L. Zhang and C.-Y. Su, *Chem. Sci.*, 2017, **8**, 775; (d) D. J. Xiao, J. Oktawiec, P. J. Milner and J. R. Long, *J. Am. Chem. Soc.*, 2016, **138**, 14371.

12 P. M. Stanley, J. Haimerl, C. Thomas, A. Urstoeger, M. Schuster, N. B. Shustova, A. Casini, B. Rieger, J. Warnan and R. A. Fischer, *Angew. Chem., Int. Ed.*, 2021, **60**, 17854.

13 P. Deria, D. A. Gómez-Gualdrón, I. Hod, R. Q. Snurr, J. T. Hupp and O. K. Farha, *J. Am. Chem. Soc.*, 2016, **138**, 14449.

14 X. Gong, Y. Shu, Z. Jiang, L. Lu, X. Xu, C. Wang and H. Deng, *Angew. Chem., Int. Ed.*, 2020, **59**, 5326.

15 K. Sasan, Q. Lin, C. Mao and P. Feng, *Chem. Commun.*, 2014, **50**, 10390.

16 Z.-B. Fang, T.-T. Liu, J. Liu, S. Jin, X.-P. Wu, X.-Q. Gong, K. Wang, Q. Yin, T.-F. Liu, R. Cao and H.-C. Zhou, *J. Am. Chem. Soc.*, 2020, **142**, 12515.

17 H.-Q. Xu, J. Hu, D. Wang, Z. Li, Q. Zhang, Y. Luo, S.-H. Yu and H.-L. Jiang, *J. Am. Chem. Soc.*, 2015, **137**, 13440.

18 P. Asselin and P. D. Harvey, *ACS Appl. Nano Mater.*, 2022, **5**, 6055.

19 S. Choi, W.-J. Jung, K. Park, S.-Y. Kim, J.-O. Baeg, C. H. Kim, H.-J. Son, C. Pac and S. O. Kang, *ACS Appl. Mater. Interfaces*, 2021, **13**, 2710.

20 H.-J. Son, S. Jin, S. Patwardhan, S. J. Wezenberg, N. C. Jeong, M. So, C. E. Wilmer, A. A. Sarjeant, G. C. Schatz, R. Q. Snurr, O. K. Farha, G. P. Wiederrecht and J. T. Hupp, *J. Am. Chem. Soc.*, 2013, **135**, 862.

21 P. M. Stanley, M. Parkulab, B. Rieger, J. Warnan and R. A. Fischer, *Faraday Discuss.*, 2021, **231**, 281.

22 G. Sahara and O. Ishitani, *Inorg. Chem.*, 2015, **54**, 5096.

23 (a) A. M. Cancelliere, F. Puntoriero, S. Serroni, S. Campagna, Y. Tamaki, D. Saito and O. Ishitani, *Chem. Sci.*, 2020, **11**, 1556; (b) P. M. Stanley and J. Warnan, *Energies*, 2021, **14**, 4260.

24 A. Gabrielsson, F. Hartl, H. Zhang, J. R. Lindsay Smith, M. Towrie, A. Vlcek and R. N. Perutz, *J. Am. Chem. Soc.*, 2006, **128**, 4253.

25 K. Kiyosawa, N. Shiraishi, T. Shimada, D. Masui, H. Tachibana, S. Takagi, O. Ishitani, D. A. Tryk and H. Inoue, *J. Phys. Chem. C*, 2009, **113**, 11667.

26 C. D. Windle, M. W. George, R. N. Perutz, P. A. Summers, X. Z. Sun and A. C. Whitwood, *Chem. Sci.*, 2015, **6**, 6847.

27 P. Lang, M. Pfrunder, G. Quach, B. Braun-Cula, E. G. Moore and M. Schwalbe, *Chem.–Eur. J.*, 2019, **25**, 4509.

28 C. D. Windle, M. V. Câmpian, A.-K. Duhme-Klair, E. A. Gibson, R. N. Perutz and J. Schneider, *Chem. Commun.*, 2012, **48**, 8189.

29 (a) Y. Kobuke, in *Non-Covalent Multi-Porphyrin Assemblies*, ed. E. Alessio, Springer-Verlag, Berlin/Heidelberg, 2006, vol. 121, pp. 49–104; (b) A. Satake and Y. Kobuke, *Tetrahedron*, 2005, **61**, 13; (c) J. Warnan, Y. Pellegrin, E. Blart and F. Odobel, *Chem. Commun.*, 2012, **48**, 675.

30 E. Rousset, D. Chartrand, I. Ciofini, V. Marvaud and G. S. Hanan, *Chem. Commun.*, 2015, **51**, 9261.

31 P. Wolf, S. L. Heath and J. A. Thomas, *Inorg. Chim. Acta*, 2003, **355**, 280.

32 D. Feng, Z.-Y. Gu, J.-R. Li, H.-L. Jiang, Z. Wei and H.-C. Zhou, *Angew. Chem., Int. Ed.*, 2012, **51**, 10307.

33 K. Epp, A. L. Semrau, M. Cokoja and R. A. Fischer, *ChemCatChem*, 2018, **10**, 3506.

34 J. Jin, *React. Kinet., Mech. Catal.*, 2020, **131**, 397.

35 J. Liang, Y.-Q. Xie, Q. Wu, X.-Y. Wang, T.-T. Liu, H.-F. Li, Y.-B. Huang and R. Cao, *Inorg. Chem.*, 2018, **57**, 2584.

36 A. Vlček, in *Photophysics of Organometallics*, ed. A. J. Lees, Springer Berlin/Heidelberg, Berlin, Heidelberg, 2010, pp. 115–158.

37 G. Lucazeau, L. Guemas and A. Novak, *Inorg. Chim. Acta*, 1976, **20**, 11.

38 (a) Y. Benseghir, A. Lemarchand, M. Duguet, P. Mialane, M. Gomez-Mingot, C. Roch-Marchal, T. Pino, M.-H. Ha-

Thi, M. Haouas, M. Fontecave, A. Dolbecq, C. Sassoye and C. Mellot-Draznieks, *J. Am. Chem. Soc.*, 2020, **142**, 9428; (*b*) X. Wang, F. M. Wisser, J. Canivet, M. Fontecave and C. Mellot-Draznieks, *ChemSusChem*, 2018, **11**, 3315; (*c*) P. Deria, W. Bury, I. Hod, C.-W. Kung, O. Karagiaridi, J. T. Hupp and O. K. Farha, *Inorg. Chem.*, 2015, **54**, 2185.

39 J. Jin, *New J. Chem.*, 2020, **44**, 15362.

40 Y. Pellegrin and F. Odobel, *C. R. Chim.*, 2017, **20**, 283.

41 (*a*) L. Favereau, A. Cnossen, J. B. Kelber, J. Q. Gong, R. M. Oetterli, J. Cremers, L. M. Herz and H. L. Anderson, *J. Am. Chem. Soc.*, 2015, **137**, 14256; (*b*) M. A. Jinks, H. Sun and C. A. Hunter, *Org. Biomol. Chem.*, 2014, **12**, 1440.

42 J. Hawecker, J.-M. Lehn and R. Ziessel, *Helv. Chim. Acta*, 1986, **69**, 1990.

43 S. Meister, R. O. Reithmeier, M. Tschurl, U. Heiz and B. Rieger, *ChemCatChem*, 2015, **7**, 690.

44 (*a*) M. Waki, M. Ikai, Y. Goto, Y. Maegawa and S. Inagaki, *Eur. J. Inorg. Chem.*, 2021, **2021**, 1624; (*b*) D.-I. Won, J.-S. Lee, J.-M. Ji, W.-J. Jung, H.-J. Son, C. Pac and S. O. Kang, *J. Am. Chem. Soc.*, 2015, **137**, 13679; (*c*) Z. Fu, X. Wang, A. M. Gardner, X. Wang, S. Y. Chong, G. Neri, A. J. Cowan, L. Liu, X. Li, A. Vogel, R. Clowes, M. Bilton, L. Chen, R. S. Sprick and A. I. Cooper, *Chem. Sci.*, 2020, **11**, 543; (*d*) B. Ma, G. Chen, C. Fave, L. Chen, R. Kuriki, K. Maeda, O. Ishitani, T.-C. Lau, J. Bonin and M. Robert, *J. Am. Chem. Soc.*, 2020, **142**, 6188.

45 D.-I. Won, J.-S. Lee, Q. Ba, Y.-J. Cho, H.-Y. Cheong, S. Choi, C. H. Kim, H.-J. Son, C. Pac and S. O. Kang, *ACS Catal.*, 2018, **8**, 1018.

46 R. Hariri and S. Dehghanpour, *Appl. Organomet. Chem.*, 2021, **35**, e6422.

47 E. E. Benson and C. P. Kubiak, *Chem. Commun.*, 2012, **48**, 7374.

48 A. A. Yakovenko, J. H. Reibenspies, N. Bhuvanesh and H.-C. Zhou, *J. Appl. Crystallogr.*, 2013, **46**, 346.

49 S. M. Shaikh, S. Ilic, B. J. Gibbons, X. Yang, E. Jakubikova and A. J. Morris, *J. Phys. Chem. C*, 2021, **125**, 22998.

50 (*a*) J. Yu, J. Park, A. van Wyk, G. Rumbles and P. Deria, *J. Am. Chem. Soc.*, 2018, **140**, 10488; (*b*) S. Goswami, I. Hod, J. D. Duan, C.-W. Kung, M. Rimoldi, C. D. Malliakas, R. H. Palmer, O. K. Farha and J. T. Hupp, *J. Am. Chem. Soc.*, 2019, **141**, 17696.

51 S. S. Rajasree, J. Yu, S. M. Pratik, X. Li, R. Wang, A. S. Kumbhar, S. Goswami, C. J. Cramer and P. Deria, *J. Am. Chem. Soc.*, 2022, **144**, 1396.

52 (*a*) V. G. Rao, B. Dhital and H. P. Lu, *Chem. Commun.*, 2015, **51**, 16821; (*b*) S. Ye, A. Kathiravan, H. Hayashi, Y. Tong, Y. Infahsaeng, P. Chabera, T. Pascher, A. P. Yartsev, S. Isoda, H. Imahori and V. Sundström, *J. Phys. Chem. C*, 2013, **117**, 6066.

53 G. Kickelbick and U. Schubert, *Chem. Ber.*, 1997, **130**, 473.

54 (*a*) R. T. Hayes, C. J. Walsh and M. R. Wasielewski, *J. Phys. Chem. A*, 2004, **108**, 2375; (*b*) J. Petersson, J. Henderson, A. Brown, L. Hammarström and C. P. Kubiak, *J. Phys. Chem. C*, 2015, **119**, 4479; (*c*) M. Morisue, N. Haruta, D. Kalita and Y. Kobuke, *Chem.–Eur. J.*, 2006, **12**, 8123; (*d*) H. Chosrowjan, S. Tanigichi, T. Okada, S. Takagi, T. Arai and K. Tokumam, *Chem. Phys. Lett.*, 1995, **242**, 644.

55 J. Karolczak, D. Kowalska, A. Lukaszewicz, A. Maciejewski and R. P. Steer, *J. Phys. Chem. A*, 2004, **108**, 4570.

56 (*a*) M. Pschenitza, S. Meister, A. von Weber, A. Kartouzian, U. Heiz and B. Rieger, *ChemCatChem*, 2016, **8**, 2688; (*b*) J. K. Nganga, C. R. Samanamu, J. M. Tanski, C. Pacheco, C. Saucedo, V. S. Batista, K. A. Grice, M. Z. Ertem and A. M. Angeles-Boza, *Inorg. Chem.*, 2017, **56**, 3214; (*c*) Y. Kou, Y. Nabetani, D. Masui, T. Shimada, S. Takagi, H. Tachibana and H. Inoue, *J. Am. Chem. Soc.*, 2014, **136**, 6021.

57 (*a*) G. Jin, D. Sensharma, N. Zhu, S. Vaesen and W. Schmitt, *Dalton Trans.*, 2019, **48**, 15487; (*b*) A. Wagner, C. D. Sahm and E. Reisner, *Nat. Catal.*, 2020, **3**, 775.

58 C. Matlachowski, B. Braun, S. Tschierlei and M. Schwalbe, *Inorg. Chem.*, 2015, **54**, 10351.